IEEE Access
Multidisciplinary | Rapid Review | Open Access Journal

Received March 2, 2020, accepted March 7, 2020, date of publication March 10, 2020, date of current version March 19, 2020.

Digital Object Identifier 10.1109/ACCESS.2020.2979880

Low-Profile Implementation of U-Shaped Power Quasi-Isotropic Antennas for Intra-Vehicle Wireless Communications

REN WANG, (Member, IEEE), JING-JING MA, CHUAN-SHENG CHEN, BING-ZHONG WANG, (Senior Member, IEEE), AND JIANG XIONG, (Member, IEEE)

Computational Electromagnetics Laboratory, Institute of Applied Physics, University of Electronic Science and Technology of China, Chengdu 610054, China

Corresponding author: Jiang Xiong (xiongjiang@uestc.edu.cn)

This work was supported by in part by the National Natural Science Foundation of China under Grant 61901086 and Grant 61571087, in part by the Postdoctoral Innovation Talents Support Program under Grant BX20180057, and in part by the China Postdoctoral Science Foundation under Grant 2018M640907.

ABSTRACT Intra-vehicle wireless communication applications, e.g. the wireless sensor network, are in need of antennas with uniformly radiated power for signal transmitting and receiving with their randomly distributed neighboring targets. This demand can be met with power quasi-isotropic antennas with low angular gain variation (*GV*). In this paper, two types of practical implementation for conventional U-shaped $\lambda/4$ resonators, which are supposed to have theoretically ideal (approaching zero) *GV* but have intrinsically low radiation resistance, have been proposed. One is a dual-layer U-shaped radiator. The extra added layer introduces a resonance that can be utilized for a good impedance matching with a commonly used 50 Ω feeding line. A two-element array model and the two-port network are used to show the working mechanism and design considerations. The other is a U-shaped RFID tag antenna, which can be considered as the miniaturized form of a U-shaped $\lambda/4$ resonator. With a structure evolution starting from a simple triple element model, the tag can have a good conjugate impedance matching with the terminated chip. Compared to their respective counterparts, both proposed antennas have the lowest measured *GV*. Meanwhile, their attracting features such as extremely low profile, small lateral size, light weight, simple configuration and fabrication process, and the possibility of a conformal implementation make them excellent candidates for future intra-vehicle wireless communications.

INDEX TERMS Electric dipoles, Internet of Vehicles (IoV), intra-vehicle wireless sensor networks, power quasi-isotropic antennas, RFID antennas.

I. INTRODUCTION

Wireless connectivity will prevail in future vehicle communications with its internal and external environments [1]–[7]. Concepts such as vehicle-to-sensor on-board (V2S), in-vehicle infotainment (IVI), human-vehicle interconnection etc. all belong to typical intra-vehicle wireless applications, and they also behave as important building blocks of the next generation Internet of Vehicles (IoV) [1], [8]–[11]. Fig. 1 illustrates a future intra-car wireless network where an electronic control unit (ECU) or vehicle's controller at the car center can communicate with sensors distributed throughout the entire car (currently there are more than 100 sensors per vehicle and the number still keeps increasing [1]). Compared with the conventional wired network, such a wireless (or at least a hybrid wired/wireless [12]) network is advantageous on the reduced weight, cost, complexity, and the increased flexibility (e.g. sensor can be in locations unreachable by wires) and vehicle intelligence [1], [4], [8], [12], [13]. Reliability of the in-car communication has been demonstrated in our previous work with the help of the recently emerging time-reversal techniques, which is quite suitable for a rich multi-path environment [14].

Apparently, in a scenario in Fig. 1, an antenna that can transmit and receive electromagnetic signals with randomly distributed neighboring targets is indispensible. This is in theory the concept of isotropic antennas. In fact, as an ideal electromagnetic isotropic source with simultaneous identical radiated power and polarization in all directions does not exist in principle, as dictated by the Maxwell equations [15],

The associate editor coordinating the review of this manuscript and approving it for publication was Shah Nawaz Burokur.

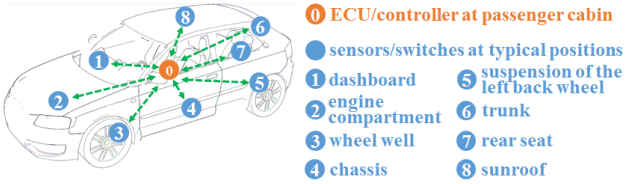

FIGURE 1. Typical wireless sensor network deployment.

a series of practical antennas with quasi-isotropic radiated power have been studied and proposed. A key figure-of-merit for evaluating the angular uniformity of the radiated power for such power quasi-isotropic radiators, i.e. the gain variation (*GV*), will be used throughout the paper. It is defined as the angular gain difference at a specific operating frequency, and it has already been widely utilized in the literature [16], [17].

Up to now, typical methods and techniques for achieving such quasi-isotropic radiation include: U-shaped λ/4 resonators [18]–[21], meander line radiators [16], [22]–[24], multiple dipole combinations [17], [25]–[27], and the recently emerging electric-magnetic dipoles [28]-[30]. Compared to the latter three categories which can mainly rely on intuition and cut and try process, only the U-shaped λ/4 resonators have been theoretically studied and exact analytical solutions have been given. In particular, it has been shown that a U-shaped λ/4 resonator with closely spaced two parallel arms has the potential of a perfect power isotropy ($GV = 0$ dB) [18], [20]. However, due to the opposite electric current on the two parallel arms, the U-shaped radiator has intrinsically low radiation resistance, leading to the impedance matching difficulty. This is a critical reason that U-shaped λ/4 resonators have not been widely applied. Recently, a U-shaped λ/4 resonator inspired sector cavity radiator has been proposed and a *GV* of 5.7 dB has been achieved [21]. However, this radiator still seems to be bulky due to its sector shape and relatively thick substrate (6 mm at 2.45 GHz).

Given the theoretically vanishing *GV* of a conventional U-shaped λ/4 resonator, we have proposed two designs as follows to make the radiator more practical, especially for the application of future intra-vehicle wireless communications. One is a dual-layer U-shaped radiator in Section II. With an additional identical U-shaped structure but of specific geometrical parameters and mutual distance, a fairly large input resistance around the introduced resonance can be utilized for the impedance matching. The almost in-phase current on the two layers renders a far-field distribution with extremely low measured *GV*. Both the working mechanism and an important parameter study have been carefully described. The other is a U-shaped RFID tag antenna in Section III, based on a triple infinitesimal current element model, which is in fact a miniaturized version of the conventional U-shaped λ/4 resonator. Compared with several other quasi-isotropic tag antennas, the proposed one also has the lowest measured *GV*. As to the two proposed quasi-isotropic antennas, the former one is comparable to wavelength and can be applied in a transceiver, and the latter is a much electrically smaller tag in an RFID system. Both designs have the advantages of light weight, simple configuration and fabrication process, and the potential of a conformal representation, all appealing features for intra-vehicle wireless communications. A conclusion will be finally given in Section IV.

II. THE DUAL-LAYER U-SHAPED RADIATOR

In this section, we show that the input resistance of a classic power isotropic U-shaped λ/4 resonator can be significantly increased for impedance matching at the operating frequency, if an additional identical layer with elaborately chosen arm length and mutual distance is utilized.

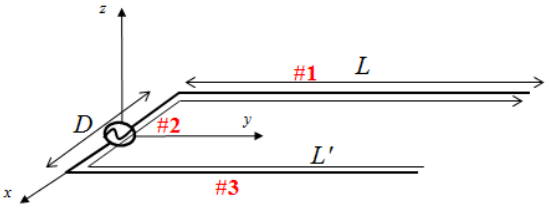

FIGURE 2. The geometry of a U-shaped λ/4 resonator fed in the center.

The geometry of a conventional U-shaped λ/4 resonator is shown in Fig. 2. It has two parallel *y*-axis directed arms and a short *x*-axis directed connecting section, which are denoted as #1 to #3 in the figure. The physical length of #1 (also #3) and #2 are L and D, respectively, and the total length of the radiator is L'. This problem has historically been studied both in the spatial and spectrum domain [18]–[20]. We here present a solution with the assumption that the center fed surface current follows a sinusoidal distribution along the entire radiator, which is more general for a flexible length of #1 to #3 (note that in [18]-[20] only the case for $L = \lambda/4$ and a vanishing D is assumed). The current distribution is explicitly written as

$$\begin{cases} \vec{I}_1 = \hat{a}_y I_0 \sin[\beta(L - y')], & x' = -\dfrac{D}{2}, 0 \le y' \le L \\ \vec{I}_2 = -\hat{a}_x I_0 \\ \quad \sin[\beta(L + \dfrac{D}{2} - |x'|)], & -\dfrac{D}{2} \le x' \le \dfrac{D}{2}, y' = 0 \\ \vec{I}_3 = -\hat{a}_y I_0 \sin[\beta(L - y')], & x' = \dfrac{D}{2}, 0 \le y' \le L, \end{cases} \tag{1}$$

where $\vec{I}_1$, $\vec{I}_2$, $\vec{I}_3$ represent the vector currents on the three sections. I_0 is the current magnitude (current maximum is at the feed), and β is the phase constant at the operating frequency. An auxiliary potential based far-field solution in the spherical coordinate system is given in (2) at the bottom of next page, where ω is the angular frequency and μ is the permeability of free space. Now the gain variation (in our theoretical analysis the radiation efficiency is assumed unity)

in terms of decibels can be defined as

$$GV(\text{dB}) = 20\log\left[\frac{\max(\left|\vec{E}(\theta,\phi)\right|)}{\min(\left|\vec{E}(\theta,\phi)\right|)}\right], \tag{3}$$

where $\vec{E}(\theta,\phi)$ is the vector sum of E_θ and E_ϕ components. A parameter study shows that when L is around $\lambda/4$ and D vanishes, GV approaches 0 dB (e.g. when $L = 0.244\lambda$ and $D = 0.012\lambda$, GV is only 0.3 dB), a result in accordance with previous findings [18]–[20].

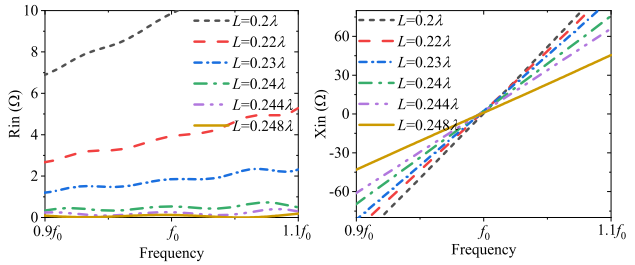

FIGURE 3. Simulated input (a) resistance and (b) reactance of a conventional U-shaped λ/4 resonator with a fixed λ/2 total length but six different arm length.

Unfortunately, despite the appealing radiation property, the low radiation resistance has severely hindered the practical application of this radiator. Fig. 3 shows the simulated input impedance at the operating frequency $f_0 = 2.4$ GHz with a gradually increased L and reduced D while the total length L' is fixed to be 0.5λ. All full wave simulations of this work were carried out with the finite integration technique based commercial software, CST Microwave Studio [31]. One sees in the figure that, though the radiator with a total length of λ/2 always has a resonance ($X_{in} = 0$) at f_0, the input resistances there are only a few ohms, and in particular, R_{in} even vanishes when $L = 0.248\lambda$ and $D = 0.004\lambda$, which is the limiting case toward a theoretical isotropic radiation [18]–[21]. Thus, it is inconvenient to match the extremely small R_{in} with a commonly used 50 Ω feeding line.

To circumvent this difficulty, a parasitic layer with an identical radiating shape is introduced, as shown in Fig. 4 (a).

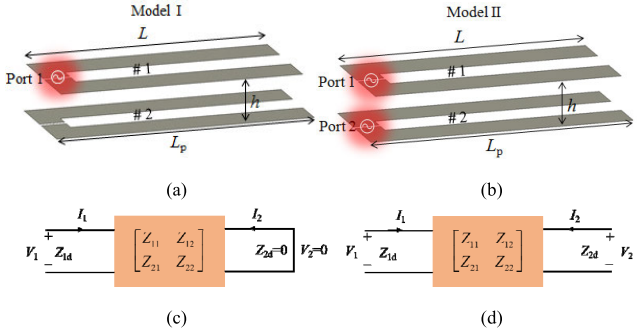

FIGURE 4. The (a) proposed dual-layer U-shaped radiator (Model I), (b) its tow-element array counterpart (Model II), and (c) and (d) their two-port network.

This two-element system, a driven element #1 and a parasitic element #2, in fact forms a canonical problem associated with mutual coupling (or mutual impedance) calculation. Although in principle it can be analytically solved e.g. with the induced EMF method [32], considering the tedious near-field calculation due to the relative complex configuration, we resort to a full-wave simulation based two-port network analysis instead. Fig. 4 (c) shows its two-port network, which is characterized by the impedance matrix [32], [33]. The input impedance, i.e. the driving-point impedance, of the dual-layer U-shaped antenna, depends upon both the self-impedance and the mutual impedance between the driven and parasitic elements. To quantitatively obtain and control the mutual impedance, an active two-element model (i.e. the parasitic element is center fed by a discrete port) was also examined, as shown in Fig. 4 (b). Its corresponding two-port network is given in Fig. 4 (d). For convenience we denote hereafter the antenna model in Fig. 4 (a) and (b) as Model I and II, respectively. A comparison with the two models indicates that port 2 is simply shorted in the practical model (Model I).

Now, the input impedance (also the driving-point impedance) of port 1, Z_{1d} in Fig. 4(c), can be calculated by

$$Z_{\text{in}} = Z_{1\text{d}} = \frac{V_1}{I_1} = Z_{11} - Z_{21}\left(\frac{Z_{21}}{Z_{11}}\right). \tag{4}$$

Note that in the last equation, $Z_{12} = Z_{21}$ and $Z_{22} \approx Z_{11}$ are applied, as the network reciprocity and the geometry

$$\begin{cases} E_\theta = \dfrac{\mathrm{j}\omega\mu I_0 e^{-\mathrm{j}\beta r}}{4\pi r}\left\{\dfrac{e^{-\mathrm{j}\beta DX/2}\left[\beta\left(e^{\mathrm{j}\beta DX}+1\right)\sin(\beta D/2)+\mathrm{j}\beta X\left(e^{\mathrm{j}\beta DX}-1\right)\cos(\beta D/2)\right]}{\beta^2(1-X^2)}\cos\theta\cos\phi\right. \\ \left. +2\mathrm{j}\dfrac{\left[\beta e^{\mathrm{j}\beta LY}-\mathrm{j}\beta Y\sin(\beta L)-\beta\cos(\beta L)\right]\sin(\beta DX/2)}{\beta^2(1-Y^2)}\cos\theta\sin\phi\right\} \\ E_\phi = \dfrac{\mathrm{j}\omega\mu I_0 e^{-\mathrm{j}\beta r}}{4\pi r}\left\{-\dfrac{e^{-\mathrm{j}\beta DX/2}\left[\beta\left(e^{\mathrm{j}\beta DX}+1\right)\sin(\beta D/2)+\mathrm{j}\beta X\left(e^{\mathrm{j}\beta DX}-1\right)\cos(\beta D/2)\right]}{\beta^2(1-X^2)}\sin\phi\right. \\ \left. +2\mathrm{j}\dfrac{\left[\beta e^{\mathrm{j}\beta LY}-\mathrm{j}\beta Y\sin(\beta L)-\beta\cos(\beta L)\right]\sin(\beta DX/2)}{\beta^2(1-Y^2)}\cos\phi\right\} \end{cases}$$
$$X = \sin\theta\cos\phi,\ Y = \sin\theta\sin\phi \tag{2}$$

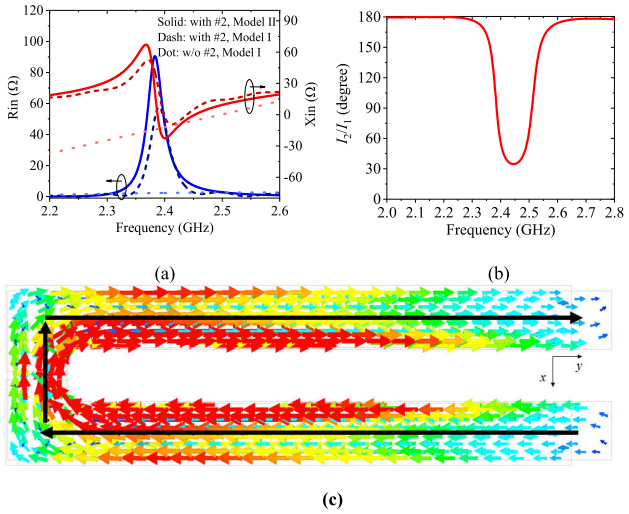

FIGURE 5. The simulated (a) input impedance, (b) current phase difference, and (c) instantaneous surface current distribution of the dual layer U-shaped λ/4 resonator. The input impedance of a conventional single layer U-shaped λ/4 resonator is also shown in (a) for comparison. The black arrows in (c) highlight the current flow direction.

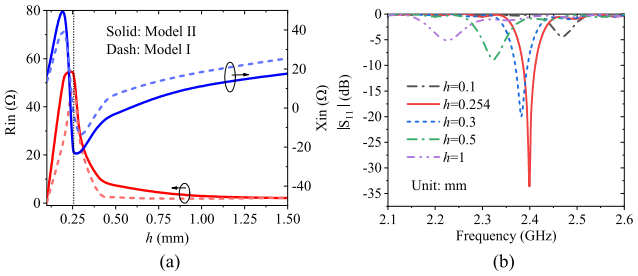

FIGURE 6. The simulated (a) input impedance at 2.4 GHz for the two models and (b) $|S_{11}|$ of Model I with a variation of h. The vertical black dash line indicates the optimal value of h.

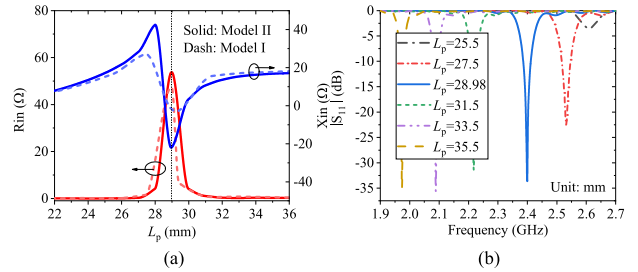

FIGURE 7. The simulated (a) input impedance at 2.4 GHz for the two models and (b) $|S_{11}|$ of Model I with a variation of L_p. The vertical black dash line indicates the optimal value of L_p.

similarity of the two layers are considered. We plot two sets of input impedance curves in Fig. 5 (a). One is from a direct simulation of Model I. The other is calculated by (4), where Z_{21} and Z_{11} are obtained by a simulation for Model II and the driven element #1 only (the parasitic element removed), respectively. These two sets of input impedance are together compared with that of a single U-shaped λ/4 resonator. Note that the latter is almost identical with the blue dash dot line (the $L = 0.23\lambda$ case) in Fig. 2. From the figure, one sees due to the mutual coupling introduced by the added layer, a resonance is introduced at f_0 where the considerably increased R_{in} can be conveniently utilized for the resistance matching. In general, the fairly good agreement between the two sets of input impedance has justified the two-port network analysis. The slight deviation arises from an additional cut at port 2 in Model II, and the approximation $Z_{22} \approx Z_{11}$ (the lengths of the two-layer radiator are close but not strictly identical).

The effectiveness of the dual-layer radiators can further be understood by an investigation on the electric currents on both layers. It can be found in Fig. 5 (b) that currents on the two layers are always out of phase except around the introduced resonance at f_0, where the current phase difference is approaching 30° (this low phase difference is almost imperceptible in the current animation). A snapshot of an instantaneous current distribution on both layers is exhibited in Fig. 5 (c) and the same flow direction on the two layers guarantees their separate radiation adds constructively in the far-field region.

We next demonstrate that a successful dual-layer U-shaped radiator design mainly relies on two elaborately chosen geometric parameters: the distance between the two layers h and the arm length of the parasitic resonator L_p. The corresponding parameter study results are summarized in Fig. 6 and 7, where L is fixed as 27.14 mm. One sees in the two figures that both the input impedance and reflection coefficient dip change dramatically once h and L_p deviate from the optimal values (denoted by the vertical dash lines). The above analysis and corresponding features, in fact, parallel to a bunch of other parasitic loaded antennas. A classic and typical example is the Yagi-Uda array, where the parasitic element length itself mainly determines the self impedance and the distance between the driven and parasitic elements significantly affects the mutual distance [32].

The final optimized geometry of the dual-layer U-shaped radiator and the fabricated prototype are shown in Fig. 8. The two layers are printed on opposite sides of a Rogers RT5880 substrate with a dielectric constant of 2.2 and a thickness of 0.254 mm.

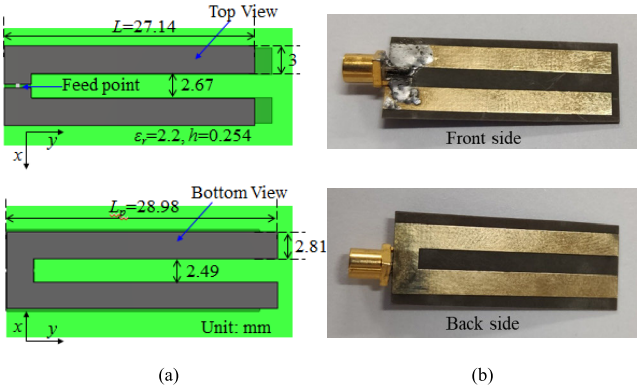

FIGURE 8. The (a) geometry and (b) fabricated prototype of the proposed dual-layer U-shaped antenna.

The reflection coefficient of the fabricated antenna prototype was measured with a domestic Ceyear 3656D network analyzer and measurement for the radiation properties was conducted in the Satimo StarLab-E multi-probe system. A micro-miniature coaxial (MMCX) connector was practically used to connect the front layer and the feeding coaxial cable, and a sleeve balun with thin copper sheet to choke current on the outer conductor of the cable was applied during measurement. The simulated and measured $|S_{11}|$, total efficiency (reflection loss included), and maximum gain (corresponding to the direction of maximum radiation at each frequency) are plotted and compared in Fig. 9, where one sees the fairly good agreement between the simulated and measured results. The simulated and measured radiation efficiencies at the frequency of best matching are 0.77 and 0.7, respectively. The simulated and measured gains at 2.4 GHz, with these finite radiation efficiencies taken into account, are then approximately −0.7 dB and −1 dB (the gain for an ideal isotropic source is 0 dB), respectively.

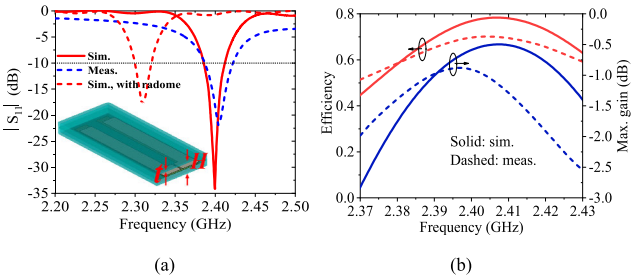

FIGURE 9. Simulated and measured (a) $|S_{11}|$, and (b) efficiency and maximum gain of the dual-layer U-shaped antenna. The inset of (a) shows a model of the antenna with an FRP ($\varepsilon_r = 3.5$, $\tan\delta = 0.01$) radome, which has a thickness of t = 0.25 mm and height of H = 2 mm.

The 3D radiation patterns at 2.4 GHz are measured and here in Fig. 10 the results only on three orthogonal planes are shown and compared with the simulated ones. It is seen that all patterns approach a circle, except a relatively larger deviation for the measured ones along *y*-axis [see Figs. 10 (a) and (c)]. The measured *GV* is correspondingly calculated to be within 3 dB, a bit larger than the simulated 1.6 dB. The fabrication tolerance, connecting cable, and rotating pedestal [see Fig. 10 (d), right along the *y*-axis] together contribute to the deviation.

A comparison for the *GV* of our proposed with that of some previously reported single band quasi-isotropic antennas is summarized in Table 1. Note that in this comparison, some quasi-isotropic antennas for dual band or multi-band applications (e.g. [27]), are not counted in due to the different design purpose, while designs with a small size especially working as radio-frequency identification (RFID) tags will be compared with our another design in the next section. In the table, one sees that our proposed U-shaped radiator has both the lowest *GV* and smallest size. In particular, this radiator is extremely low-profile and lightweight, compared with those bulky designs and most of its planar counterparts in the table. A corresponding conformal version can be expected via a quick optimization. For a complete comparison we have also listed the bandwidth performance (note that for almost all reference only the impedance bandwidth is available and thus the reported measured *GV* does not necessarily represent the

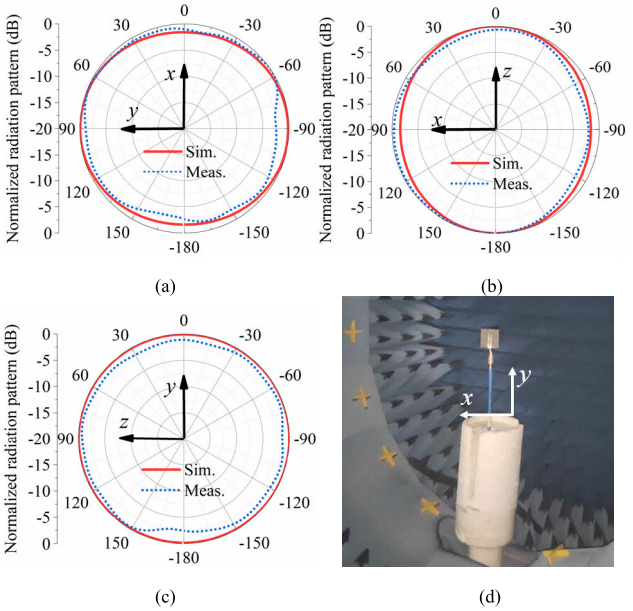

FIGURE 10. Simulated and measured normalized pattern of the dual-layer U-shaped antenna on the (a) *x*-*y* plane, (b) *x*-*z* plane, and (c) *y*-*z* plane at 2.4 GHz. (d) Scenario of the radiation pattern measurement.

TABLE 1. GV comparison of some quasi-isotropic antennas.

Technique	Ref.	Configuration Size (λ_0^3)	-10dB BW	*GV* (dB)	
				Sim	Meas
meandering dipoles	[22]	spherical, bulky 0.1(radius)^3	5.3%	3	N/A
crossed dipoles	[25]	rectangular, planar 0.256×0.256×0.008	11%	3.7	6.67
	[26]	rectangular, planar 0.37×0.37×0.007	20.8%	5.75	6
complementary electric-magnetic dipoles	[29]	cylinder, bulky π×0.12(radius)^2 ×0.1(height)	7%	7.5	7.9
	[30]	rectangular, bulky 0.22×0.22×0.12	6.9%	3.4	5.6
U-shaped λ/4 resonators	[21]	sector cylinder, bulky π×0.2(radius)^2×0.05(height)	4.1%	1.8	5.7
	This work	**rectangular, planar 0.23×0.06×0.002**	**1.6%**	**1.6**	**3**

GV level within the entire band), and the limited bandwidth is due to the intrinsic resonance mechanism.

Finally, we have also studied the antenna property if it is enclosed by a radome in practical applications. The inset of Fig. 9 (a) shows the CST model for the U-shaped antenna with a fiber reinforced plastics (FRP) box. The FRP is commonly used material for radomes due to its excellent mechanical strength and heat resistance, and it has a dielectric constant of 3.5 and loss tangent of 0.01. One sees in the figure that when a typical 0.25 mm thick, 2 mm height FRP radome is applied, the antenna has a lower resonance. Our simulation study shows that the resonance shift increases with a larger material dielectric constant, and a smaller radome size (i.e. a reduced distance between the radome wall and the radiator, characterized by the box height H) will simultaneously lead to the resonance shift and a slightly increased *GV*. This suggests an appropriate tradeoff between the radome volume and the *GV* performance. Once the radome parameters are determined, the operating frequency can be conveniently tuned back with a fast optimization on the antenna geometrical parameters. The existence of the radome, due to the modest material loss tangent and very thin shell, has trivial effect on the radiation efficiency and gain.

III. THE U-SHAPED RFID TAG ANTENNA

As an important composing technology for future intra-vehicle systems [1], [8], RFID and the tag antennas with quasi-isotropic property also attract intense interest in the literature [16], [23], [24], [34], [35]. In view of the working mechanism of the U-shaped λ/4 resonators, it is straightforward to anticipate a similar power isotropy property when the radiator size is substantially reduced. Fig. 11 shows another U-shaped radiator model but formed by three separate infinitesimal current elements. The three sections are still denoted by #1 to #3. Due to the infinitesimal length l, currents along #1 to #3 are assumed constant and they are related by $I_1 = I_3 = kI_2$. Now the far-field solution is given in (5) at the bottom of this page. A minimal *GV* via particle swarm optimization (PSO) is found to be as low as 0.014 dB when $k = 4.494$, $d_x = 0.035\lambda$, and $d_y = 0.081\lambda$.

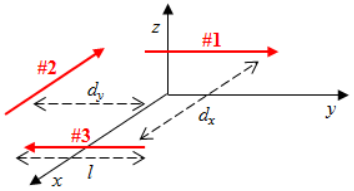

FIGURE 11. The U-shaped radiator model composed of three separate infinitesimal current elements.

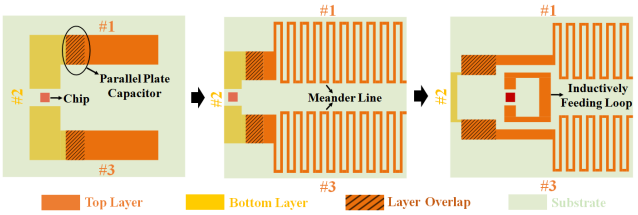

FIGURE 12. Structure evolution of a U-shaped RFID tag antenna.

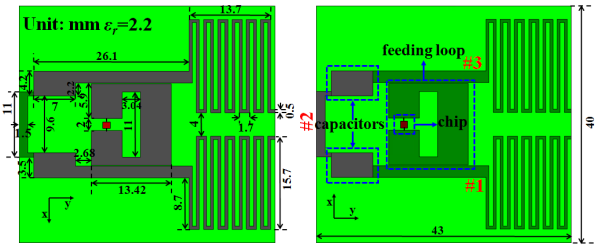

FIGURE 13. A (a) top and (b) bottom view of the proposed U-shaped RFID tag antenna.

A power quasi-isotropic RFID tag antenna can thus be designed from this model and Fig. 12 illustrates the design procedure. Firstly, all three current elements in Fig. 11 were represented by metallic strips with finite but small length and width on the substrate, and an Impinj Monza4 chip with an impedance of 11-j143 Ω is placed at the middle of #2. Note that #2 was etched on the opposite side of #1 and #3 so that the partially overlapped sections (see the shaded area in the figure) form capacitors and the couplings can be regulated for a required current ratio k. Next, meander lines were utilized at the "U" ends for a sufficiently large inductance for conjugate impedance matching. Finally, a small loop has been utilized as an inductive feed to reduce the meander line numbers and the total tag size. It also helps increase the regulation freedom.

The optimized U-shaped RFID tag antenna with detailed dimensions is shown in Fig. 13. The simulated current distribution on the tag antenna is shown in Fig. 14 (a). The black arrows help indicate the current flow on the three sections, and one sees it is consistent with that in Fig. 11. Extracted current magnitude and phase on #1 and #2 are plotted in Fig. 14 (b), where one sees the current on these two sections are of a certain difference in magnitude (representing the current ratio k) but strictly in phase. The magnitude fluctuation is due to the fact that the current vector is not

$$\begin{cases} E_\theta = \dfrac{\mathrm{j}\omega\mu I_1 e^{-\mathrm{j}\beta r}}{2\pi\beta r}\left[\dfrac{\sin(\beta lX/2)\, e^{-\mathrm{j}\beta d_y Y}}{kX}\cos\theta\cos\phi + 2\mathrm{j}\dfrac{\sin(\beta lY/2)\sin(\beta d_x X/2)}{Y}\cos\theta\sin\phi\right] \\ E_\phi = -\dfrac{\mathrm{j}\omega\mu I_1 e^{-\mathrm{j}\beta r}}{2\pi\beta r}\left[\dfrac{\sin(\beta lX/2)\, e^{-\mathrm{j}\beta d_y Y}}{kX}\sin\phi - 2\mathrm{j}\dfrac{\sin(\beta lY/2)\sin(\beta d_x X/2)}{Y}\cos\phi\right] \end{cases} \tag{5}$$

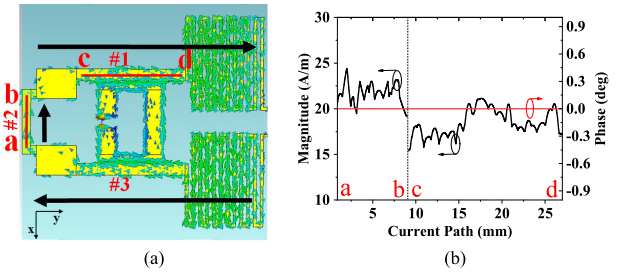

(a) (b)

FIGURE 14. Simulated (a) current vector distribution and (b) extracted current magnitude and phase along #1 and #2. The black arrows in (a) highlight the current flow directions.

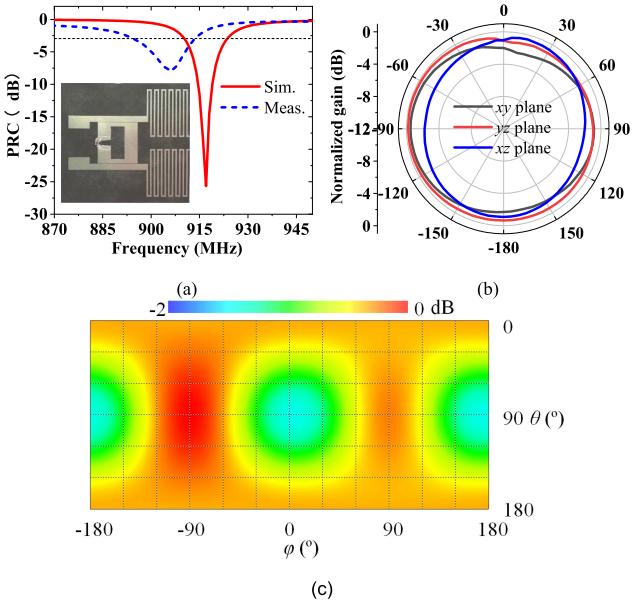

FIGURE 15. Simulated and measured (a) power reflection coefficient and (b) normalized gain pattern on three orthogonal planes of the proposed U-shpaed RFID tag antenna. The fabricated tag antenna with a chip is shown in the inset of (a). In (b), the angular variables for three planes in a spherical coordinate system are ϕ for the *x-y* plane, and θ for the *y-z* and *x-z* planes, respectively. (c) The simulated 2D power pattern of the tag.

necessarily along the current extraction line [see the red solid lines in Fig. 14 (a)] in CST. Also note that the x-axis directed currents on the neighboring thin strips of the meander lines cancel each other and eventually do not produce notable radiation.

Fig. 15 summarizes the simulated and measured performances of the tag antenna. The fabricated tag is shown in the inset of (a). Based on the input impedance characterization technique in [36], the power reflection coefficient (PRC) was measured and one sees in Fig. 15 (a) that the fabricated tag antenna operates at 906 MHz, slightly lower than the simulated 915 MHz. A horizontal line in the figure indicates a PRC of −3 dB, which is a well accepted standard for RFID tags. The radiation property was measured with a Hand Carry Kit UHF of the Voyantic Tagformance Pro Measurement System. The gain can be calculated via the orientation sensitivity measurement program in the instrument [37]. Since polarization of this tag antenna is orientation dependent [20], partial gains for the two orthogonal polarizations in each direction have been recorded and then added to obtain the actual gain [32]. A complete 3D measurement for the pattern of a tag antenna (terminated with a chip) is quite difficult, and therefore, as a common practice in the community, the tag antenna response was measured for three orthogonal planes. The measured normalized gain patterns are plotted in Fig. 15 (b) and the maximum *GV* is within 2.8 dB, representing good isotropy property. For a comparison, a simulated 2D plot of the normalized 3D radiated power is shown in Fig. 15 (c) and the simulated *GV* is 2 dB. The simulated gain is −3.6 dBi, which is a typical value for tag antenna [16]. A measured read range of 2.22-2.62 m has been achieved when an effective isotropic radiated power (EIRP) of 0.5 W was applied.

TABLE 2. comparison of the size and measured GV of some quasi-isotropic RFID tag antennas.

Ref.	Size	*GV* (dB)		Orthogonal Planes Investigated
		Sim	Meas	
[16]	$0.20\lambda_0\times0.20\lambda_0$	2.73	6.0	3
[23]	$0.12\lambda_0\times0.14\lambda_0$	6.33	3.1	3
[24]	$0.13\lambda_0\times0.09\lambda_0$	2.6	N/A	2
[34]	$0.16\lambda_0\times0.24\lambda_0$	3	4.5	N/A
[35]	$(0.038\lambda_0)^3$ (sphere)	5	N/A	3
This work	$\mathbf{0.12\lambda_0\times0.13\lambda_0}$	**2**	**2.8**	**3**

The size and *GV* are compared with some reported quasi-isotropic RFID tag antennas (all balun free) and the results are summarized in Table 2. During our design, the antenna size was intentionally restricted to be similar to its counterparts. Again we have achieved the lowest measured *GV*. As a final remark, although the current tag antenna was designed without considering the surrounding environment, an easy co-design with the affixing platform, based on a good understanding of the U-shaped antenna radiation mechanism, can be expected.

IV. CONCLUSION

This work aims to push the classical U-shaped λ/4 resonators toward a more practical implementation for a wide range of applications. Particularly, their low profile and ideal power isotropy features are appealing to the flourishing intra-vehicle wireless communications. Two U-shaped antennas, one with electrically medium size and considerable radiation efficiency for a 50 Ω impedance matching and the other with electrically small size for a conjugate impedance matching to a tag chip, have been proposed. The working principle and design guidelines for both designs have been illustrated. A brief performance analysis for the antenna enclosed by a practical radome has also been given. Measured performance shows that both low-profile antennas have good impedance matching and pretty low *GV*, which make them promising for future intra-vehicle wireless communications.

ACKNOWLEDGMENT

The authors are thankful to HWA-TECH for its support on our RFID tag antenna measurement.

REFERENCES

[1] N. Lu, N. Cheng, N. Zhang, X. Shen, and J. W. Mark, "Connected vehicles: Solutions and challenges," *IEEE Internet Things J.*, vol. 1, no. 4, pp. 289–299, Aug. 2014.
[2] M. Gerla, E.-K. Lee, G. Pau, and U. Lee, "Internet of vehicles: From intelligent grid to autonomous cars and vehicular clouds," in *Proc. IEEE World Forum Internet Things (WF-IoT)*, Seoul, South Korea, Mar. 2014, pp. 241–246.
[3] D. Kombate and L. Wang, "The Internet of vehicles based on 5G communications," in *Proc. IEEE Int. Conf. Internet Things (iThings) IEEE Green Comput. Commun. (GreenCom) IEEE Cyber, Phys. Social Comput. (CPSCom) IEEE Smart Data (SmartData)*, Chengdu, China, Dec. 2016, pp. 445–448.
[4] D. W. Matolak and A. Chandrasekaran, "5 GHz intra-vehicle channel characterization," in *Proc. IEEE Veh. Technol. Conf. (VTC Fall)*, Sep. 2012, pp. 1–5.
[5] L. Chi, Y. Qi, Z. Weng, W. Yu, and W. Zhuang, "A compact wideband slot-loop directional antenna for marine communication applications," *IEEE Trans. Veh. Technol.*, vol. 68, no. 3, pp. 2401–2412, Mar. 2019.
[6] Z.-P. Zhong, X. Zhang, J.-J. Liang, C.-Z. Han, M.-L. Fan, G.-L. Huang, W. Xu, and T. Yuan, "A compact dual-band circularly polarized antenna with wide axial-ratio beamwidth for vehicle GPS satellite navigation application," *IEEE Trans. Veh. Technol.*, vol. 68, no. 9, pp. 8683–8692, Sep. 2019.
[7] S. Wang, L. Zhu, G. Zhang, J. Yang, J. Wang, and W. Wu, "Dual-band dual-CP all-metal antenna with large signal coverage and high isolation over two bands for vehicular communications," *IEEE Trans. Veh. Technol.*, vol. 69, no. 1, pp. 1131–1135, Jan. 2020.
[8] T. ElBatt, C. Saraydar, M. Ames, and T. Talty, "Potential for intra-vehicle wireless automotive sensor networks," in *Proc. IEEE Sarnoff Symp.*, Princeton, NJ, USA, Mar. 2006, pp. 1–4.
[9] K. M. Alam, M. Saini, and A. E. Saddik, "Toward social Internet of vehicles: Concept, architecture, and applications," *IEEE Access*, vol. 3, pp. 343–357, 2015.
[10] P. H. L. Rettore, A. B. Campolina, L. A. Villas, and A. A. F. Loureiro, "A method of eco-driving based on intra-vehicular sensor data," in *Proc. IEEE Symp. Comput. Commun. (ISCC)*, Heraklion, Greece, Jul. 2017, pp. 1122–1127.
[11] P. H. L. Rettore, A. B. Campolina, A. Souza, G. Maia, L. A. Villas, and A. A. F. Loureiro, "Driver authentication in VANETs based on intra-vehicular sensor data," in *Proc. IEEE Symp. Comput. Commun. (ISCC)*, Natal, Brazil, Jun. 2018, pp. 78–83.
[12] W. Si, D. Starobinski, and M. Laifenfeld, "A robust load balancing and routing protocol for intra-car hybrid Wired/Wireless networks," *IEEE Trans. Mobile Comput.*, vol. 18, no. 2, pp. 250–263, Feb. 2019.
[13] A. R. Moghimi, H.-M. Tsai, C. U. Saraydar, and O. K. Tonguz, "Characterizing intra-car wireless channels," *IEEE Trans. Veh. Technol.*, vol. 58, no. 9, pp. 5299–5305, Nov. 2009.
[14] R. Wang, B.-Z. Wang, Z.-S. Gong, and X. Ding, "Compact multiport antenna with radiator-sharing approach and its performance evaluation of time reversal in an intra-car environment," *IEEE Trans. Antennas Propag.*, vol. 63, no. 9, pp. 4213–4219, Sep. 2015.
[15] H. F. Mathis, "A short proof that an isotropic antenna is impossible," *Proc. IRE*, vol. 39, no. 8, p. 970, Aug. 1951.
[16] L. Liang and S. V. Hum, "A low-profile antenna with quasi-isotropic pattern for UHF RFID applications," *IEEE Antennas Wireless Propag. Lett.*, vol. 12, pp. 210–213, 2013.
[17] C. Deng, Y. Li, Z. Zhang, and Z. Feng, "A wideband isotropic radiated planar antenna using sequential rotated L-Shaped monopoles," *IEEE Trans. Antennas Propag.*, vol. 62, no. 3, pp. 1461–1464, Mar. 2014.
[18] R. Guertler, "Isotropic transmission-line antenna and its toroid-pattern modification," *IEEE Trans. Antennas Propag.*, vol. 25, no. 3, pp. 386–392, May 1977.
[19] H. Matzner, M. Milgrom, and S. Shtrikman, "A study of finite size power isotropic radiators," in *Proc. 18th Conv. Electr. Electron. Eng.*, Jerusalem, Israel, 1995, Art. no. 5176486.
[20] H. Matzner and E. Levine, "Can λ/4 radiators be really isotropic?" *Int. J. Antennas Propag.*, vol. 2012, Jan. 2012, Art. no. 187123.
[21] Q. Li, W.-J. Lu, S.-G. Wang, and L. Zhu, "Planar quasi-isotropic magnetic dipole antenna using fractional-order circular sector cavity resonant mode," *IEEE Access*, vol. 5, pp. 8515–8525, 2017.
[22] A. Mehdipour, H. Aliakbarian, and J. Rashed-Mohassel, "A novel electrically small spherical wire antenna with almost isotropic radiation pattern," *IEEE Antennas Wireless Propag. Lett.*, vol. 7, pp. 396–399, 2008.
[23] J. Ahn, H. Jang, H. Moon, J.-W. Lee, and B. Lee, "Inductively coupled compact RFID tag antenna at 910 MHz with near-isotropic radar cross-section (RCS) patterns," *IEEE Antennas Wireless Propag. Lett.*, vol. 6, pp. 518–520, 2007.
[24] S.-L. Chen, K.-H. Lin, and R. Mittra, "Miniature and near-3D omnidirectional radiation pattern RFID tag antenna design," *Electron. Lett.*, vol. 45, no. 18, pp. 923–924, 2009.
[25] G. Pan, Y. Li, Z. Zhang, and Z. Feng, "Isotropic radiation from a compact planar antenna using two crossed dipoles," *IEEE Antennas Wireless Propag. Lett.*, vol. 11, pp. 1338–1341, 2012.
[26] C. Deng, Y. Li, Z. Zhang, and Z. Feng, "A circularly polarized pattern diversity antenna for hemispherical coverage," *IEEE Trans. Antennas Propag.*, vol. 62, no. 10, pp. 5365–5369, Oct. 2014.
[27] Z. Su, K. Klionovski, R. M. Bilal, and A. Shamim, "A dual band additively manufactured 3-D antenna on package with near-isotropic radiation pattern," *IEEE Trans. Antennas Propag.*, vol. 66, no. 7, pp. 3295–3305, Jul. 2018.
[28] C.-H. Wu and T.-G. Ma, "Miniaturized self-oscillating active integrated antenna with quasi-isotropic radiation," *IEEE Trans. Antennas Propag.*, vol. 62, no. 2, pp. 933–936, Feb. 2014.
[29] P. F. Hu, Y. M. Pan, X. Y. Zhang, and B. J. Hu, "A compact quasi-isotropic dielectric resonator antenna with filtering response," *IEEE Trans. Antennas Propag.*, vol. 67, no. 2, pp. 1294–1299, Feb. 2019.
[30] Y.-M. Pan, K. W. Leung, and K. Lu, "Compact quasi-isotropic dielectric resonator antenna with small ground plane," *IEEE Trans. Antennas Propag.*, vol. 62, no. 2, pp. 577–585, Feb. 2014.
[31] (Aug. 20, 2019). *CST Studio Suite: Electromagnetic Field Simulation Software*. [Online]. Available: https://www.cst.com/
[32] C. A. Balanis, *Antenna Theory: Analysis and Design*, 3rd ed. New York, NY, USA: Wiley, 2005.
[33] D. M. Pozar, *Microwave Engineering*, 4th ed. New York, NY, USA: Wiley, 2012.
[34] C. Cho, H. Choo, and I. Park, "Broadband RFID tag antenna with quasi-isotropic radiation pattern," *Electron. Lett.*, vol. 41, no. 20, pp. 1091–1092, 2005.
[35] H.-K. Ryu, G. Jung, D.-K. Ju, S. Lim, and J.-M. Woo, "An electrically small spherical UHF RFID tag antenna with quasi-isotropic patterns for wireless sensor networks," *IEEE Antennas Wireless Propag. Lett.*, vol. 9, pp. 60–62, 2010.
[36] X. Qing, C. Khan Goh, and Z. Ning Chen, "Impedance characterization of RFID tag antennas and application in tag co-design," *IEEE Trans. Microw. Theory Techn.*, vol. 57, no. 5, pp. 1268–1274, May 2009.
[37] (May 13, 2019). *RFID Test Solution*. [Online]. Available: http://www.hwa-tech.com/en/RFID/

REN WANG (Member, IEEE) was born in Anhui, China, in 1990. He received the B.S. and Ph.D. degrees in electronic information science and technology and radio physics from the University of Electronic Science and Technology of China (UESTC), Chengdu, in 2014 and 2018, respectively. He worked at the Optoelectronics Research Centre, University of Southampton, U.K., as a Visiting Scholar, from September 2016 to September 2017. He is currently a Research Fellow at UESTC. His main research interests include phased arrays, metasurfaces, and time-reversed electromagnetics.

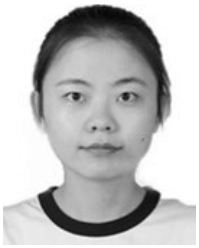

JING-JING MA was born in Shanxi, China, in 1993. She received the B.S. degree in electronic information science and technology from Shanxi University, Taiyuan, China, in 2017. She is currently pursuing the M.S. degree in radio physics with the University of Electronic Science and Technology of China (UESTC). Her research interests include computational electromagnetics and antennas with low directivity.

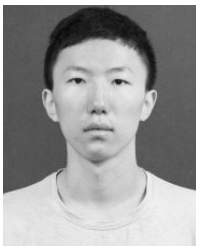

CHUAN-SHENG CHEN was born in Jilin, China, in 1997. He received the B.S. degree in electronic information science and technology from the University of Electronic Science and Technology of China (UESTC), Chengdu, China, in 2019, where he is currently pursuing the Ph.D. degree in radio physics. His research interests include computational electromagnetics and time-reversed electromagnetics.

BING-ZHONG WANG (Senior Member, IEEE) received the Ph.D. degree in electronic engineering from the University of Electronic Science and Technology of China (UESTC), Chengdu, in 1988.

In 1984, he joined UESTC, where is currently a Professor. He has been a Visiting Scholar with the University of Wisconsin–Milwaukee, WI, USA, a Research Fellow with the City University of Hong Kong, Hong Kong, China, and a Visiting Professor with the Electromagnetic Communication Laboratory, Pennsylvania State University, State College, PA, USA. His current research interests are in the areas of computational electromagnetics, antenna theory and techniques, and time-reversed electromagnetics.

JIANG XIONG (Member, IEEE) was born in Chengdu, China, in 1982. He received the B.S. degree in applied physics from the University of Electronic Science and Technology of China (UESTC), China, in 2005, and the Ph.D. degree in electronics science and technology from Zhejiang University (ZJU), China, in 2010. He is currently an Associate Professor with the Computational Electromagnetics Laboratory, Institute of Applied Physics, UESTC. His current research interests include artificial electromagnetic structures, novel antennas for modern wireless communications, electrically small antennas, and scattering.